Spectrochimica Acta Part A: Molecular and Biomolecular Spectroscopy 327 (2025) 125326

Contents lists available at ScienceDirect

Spectrochimica Acta Part A: Molecular and Biomolecular Spectroscopy

journal homepage: www.journals.elsevier.com/spectrochimica-acta-part-a-molecular-and-biomolecular-spectroscopy

A new approach to assess post-mortem interval: A machine learning-assisted label-free ATR-FTIR analysis of human vitreous humor

Valentina Notarstefano [a,*,1], Chiara Santoni [a,1], Eva Montanari [b,*], Francesco Paolo Busardò [c], Angelo Montana [c], Giulia Orilisi [d], Paolo Mariani [a], Elisabetta Giorgini [a]

[a] Department of Life and Environmental Sciences, Polytechnic University of Marche, Via Brecce Bianche, 60131 Ancona, Italy
[b] Azienda Ospedaliero-Universitaria delle Marche, Via Conca 71, 60121 Ancona, Italy
[c] Department of Biomedical Sciences and Public Health, Polytechnic University of Marche, Via Conca 71, 60121 Ancona, Italy
[d] Department of Odontostomatologic and Specialized Clinical Sciences, Polytechnic University of Marche, Via Conca 71, 60121 Ancona, Italy

HIGHLIGHTS

- Vitreous humor is very useful in the assessment of short post-mortem intervals.
- ATR-FTIR spectroscopy is able to assess post-mortem interval from vitreous humor.
- Relevant and diverse biological mechanisms can be unveiled at the same time.
- ATR-FTIR and chemometrics/machine learning are powerful in studying biofluids.

GRAPHICAL ABSTRACT

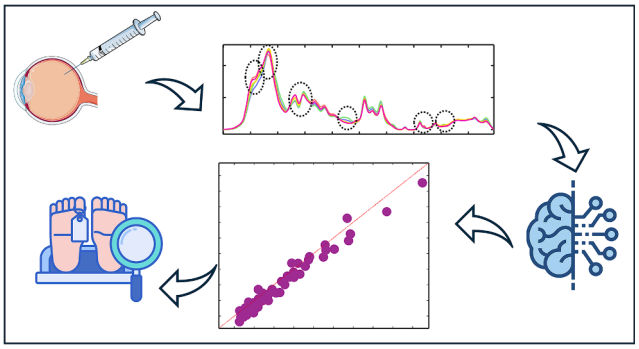

ARTICLE INFO

Keywords:
Post-mortem interval
Vitreous humor
ATR-FTIR spectroscopy
Multivariate analysis
Data mining

ABSTRACT

A crucial issue in forensics is determining the post-mortem interval (PMI), the time between death and the finding of a body. Despite various methods already employed for its estimation, only approximate values are currently achievable. Vitreous humor (VH) is an avascular tissue between the lens and the retina, mainly composed by a collagen fibers network, hyaluronic acid, and hyalocytes. Recently, it has received interest in forensic medicine, being easy to collect and susceptible to low microbiological contamination and putrefaction. Based on this evidence and thanks to the ability of Attenuated Total Reflectance – Fourier Transform InfraRed (ATR–FTIR) spectroscopy to perform fast analyses on a minimal sample amount, in this study, a new analytical approach to reliably estimate PMI is proposed combining ATR-FTIR analysis of VH human samples with multivariate statistical procedures, such as Principal Component Analysis (PCA) and Partial Least Squares-Discriminant Analysis (PLS-DA), for discriminant classification. Regression procedures, including Partial Least Squares Regression (PLSR), were performed: extremely positive results were obtained, and the most discriminant spectral features were highlighted (peaks at 1665, 1630, 1585, 1400, 1220, 1200, 1120, 854, 835, and 740 cm^{-1}) and associated to PMI classes (average accuracy over 80 %). Specific and reliable markers able to correlate the

* Corresponding authors.
E-mail addresses: v.notarstefano@univpm.it (V. Notarstefano), eva.montanari@ospedaliriuniti.marche.it (E. Montanari).
[1] These authors contributed equally.

https://doi.org/10.1016/j.saa.2024.125326
Received 25 July 2024; Received in revised form 13 October 2024; Accepted 20 October 2024
Available online 24 October 2024

macromolecular composition of VH with the PMI were identified, revealing a post-mortem protein degradation and amino acids deamination (decrease of proteins and increase of free amino acids and NH3), an increase of lactate, which diffuses from the retina to the VH, and changes in the hyaluronic acid component.

1. Introduction

Post-mortem interval (PMI), or time since death (TSD), is defined as the time elapses between death and finding a body; its accurate estimation is an important issue in forensic medicine as it can be a crucial parameter in criminal prosecution [1,2]. It sheds light on potential murder suspects during forensic investigations, contributing also to determine the possible causes of death [1].

To date, various conventional methods are available to estimate the time since death, such as the Algor mortis, based on the body's cooling after death caused by the lack of circulating blood in the vessels and the loss of regulatory mechanisms of the body temperature; this approach is considered the most accurate method of estimating the early PMI, together with the progression and regression of Rigor Mortis that occurs when the muscles become stiff due to the loss of adenosine triphosphate (ATP), and the development of Livor Mortis consisting in the collection of blood in skin vessels in the lower part of the dead body from 6 to 12 h after death [1,3]. Other methods of estimating TSD include the biochemical analysis of biofluids and entomology (examination of different types of insects found inside or outside the body); both biochemical analyses and conventional methods can provide reliable data within 1–3 days, while entomological evidence may extend the estimated time since death to several weeks or even months [4].

However, all these methods are often imprecise and influenced by climatic and environmental conditions, as well as by the experience and subjectivity of the forensic pathologist making the assessments [2]. Therefore, the accurate estimation of the PMI requires new approaches that are both fast and reliable and not subjected to external variability [1,2].

Fourier Transform InfraRed Spectroscopy (FTIR) is a powerful vibrational technique able to provide information about the macromolecular composition of the biological sample analyzed [5]. This spectroscopic approach, and more particularly Attenuated Total Reflectance – Fourier Transform InfraRed (ATR-FTIR) spectroscopy, presents several advantages over other analytical techniques. ATR-FTIR let perform fast and non-destructive analysis on a great variety of samples, both liquids and solids, with a great reproducibility and little to no chance of operator error, since minimal sample preparation is required [6]. By a single acquisition, it is possible to obtain a high-quality IR spectrum which can provide the chemical fingerprint of the sample [7]. In recent years, ATR-FTIR has been successfully applied in forensic medicine for several purposes, including the determination of the phenotype profiling of the victim, the identification and differentiation between stains of all body fluids and for toxicology analyses [8–10]. ATR-FTIR spectroscopy has also been exploited in combination with chemometric methods to estimate the post-mortem interval, by analyzing soft-tissues (adipose tissue, liver), body fluids (plasma, pericardial fluid, vitreous humor), annular cartilage, and bones [2,11–16]. Another vibrational spectroscopic technique, Raman spectroscopy, is considered very useful in PMI assessment. Both IR and Raman spectroscopy let obtain the fingerprint of biological molecules of interest in a label-free way [17], but are mutually complementary, given the different physical origin of their functioning and their sensitiveness to different classes of vibrations (IR absorption is sensitive to antisymmetric/polar group vibrations, Raman is sensitive to symmetric/polarizable ones) [17]. In the present work, the choice fell on infrared spectroscopy, in the ATR setup, since its ease of use makes it particularly suitable for an implementation into non-expert laboratories.

A useful biological matrix employed for PMI estimation, not only with infrared spectroscopy [18–21], but also with other X-ray-based techniques [22,23], is bone. In fact, bone remains are useful for toxicological and genetic analysis and evaluation [24]. Although the degradation of skeletal samples is known to be severely affected by environmental factors (i.e. bacteria, weather, and soil composition) [24], the literature reports strong evidence of the reliability of their use for PMI estimation.

Vitreous humor can be considered an interesting sample for forensic investigations. In fact, it is a transparent biological matrix placed between the lens and the retina, and therefore not very susceptible to chemical changes due to microbiological contamination, putrefaction and autolysis, which could influence the analysis and the reliability of the results [25,26]. It is mostly composed by water (>98 %) and other molecules such as collagen fibers, hyaluronic acid (the most abundant glycosaminoglycan of the VH), hyalocytes, inorganic salts and organic components [25,27,28]. The spectroscopic characterization of bone tissue is particularly useful when the PMI is in the order of years and months; analyses based on microbial investigations report an accuracy in the order of days [29]. On the contrary, the biochemical analyses performed on biological fluids, like blood, serum, and also VH, including the few studies using ATR-FTIR on this latter matrix, report an accuracy in the order of hours [2,29]. This aspect, together with the evidence that biochemical assays performed on VH, including the evaluation of potassium, hypoxanthine, and glucose levels, severely lose their accuracy as degradation advances, making this sample type more suitable for short PMIs [24,30].

Among the techniques used for biochemical and metabolic investigations, ATR-FTIR stands as particularly useful. In fact, the widely and routinely employed biochemical assays, besides being well-characterized and reliable, require kits and reagents specifically targeted towards a molecule or a class of molecules. On the contrary, this spectroscopic approach, combined with a fine statistical analysis, which can be hopefully automated within a software for laboratory routines, lets obtain on the same sample, at the same time, and in a label-free way, the complete information of the sample in study: in this way, more than one class of molecules can be analyzed and diverse metabolic pathways can be investigated.

To the best of Authors' knowledge, only three studies are reported in literature exploiting ATR-FTIR on rabbit vitreous humor, among which only one aims to find a correlation between its spectral features with the causes of death and the post mortem interval [2,31,32], while just one paper describes the application of this spectroscopic technique on human vitreous humor samples to assess the PMI *in vitro*, but only three samples were included [10]. On the other hand, Raman spectroscopy has been more widely applied to VH samples, to study, for example, the modifications occurring in this biological matrix due to diabetic retinopathy [33] and to perform a differential diagnosis between experimental endophthalmitis and uveitis [34].

Based on this evidence, in the present study we have developed a reliable analytical method for the detection of the post-mortem interval, to be applied in forensic medicine, based on the analysis of human vitreous humor. To this purpose, a significant number of human vitreous humor samples have been collected and analyzed by combining ATR-FTIR spectroscopy with a data mining approach.

2. Materials and methods

2.1. Sample collection

N. 70 human vitreous humor (VH) samples were obtained from the archive of the Department of Forensic Medicine, "Ospedali Riuniti"

General Hospital (Ancona, Italy). Samples were collected in the range of 2.5–187 h postmortem, and the age of donors ranged between 31 and 99 years. Only non-toxicological and non-infective causes of death were taken into account. After collection, VH samples were immediately stored at −80 °C in 5-ml labelled vacutainer tubes until the analysis; no fixing procedure was performed. VH samples were divided into N. 5 classes, according to the PMI: Class 1 < 10.00 h; Class 2 = 10.33–20.00 h; Class 3 = 20.83–40.00 h; Class 4 = 41.00–80.00 h; Class 5 > 81.00. Table S1 summarizes data related to sex, age, and exact PMI of the donors of the VH samples employed in the study.

2.2. ATR-FTIR acquisitions and processing

The infrared analysis was performed at the Advanced Research Instrumentation Laboratory – Polytechnic University of Marche (Ancona, Italy). ATR-FTIR spectra were acquired by a Platinum ATR accessory mounting a diamond crystal and coupled with a Bruker INVENIO-R interferometer and a Deuterated TriGlycine Sulfate (DTGS) detector (Bruker Optics, Ettlingen, Germany). Samples were dropped layering N. 3 aliquots of 4 μl onto the diamond crystal and dried by nitrogen blowdown. IR spectra were collected every 30 s until complete dehydration of samples, as monitored by the disappearance of the band at ~2100 cm^{-1} originated from the free water content. For each sample, ATR-FTIR spectra were collected at room temperature in the 4000–700 cm^{-1} range (256 scans, 4 cm^{-1} spectral resolution). Before each sample acquisition, the spectrum of the background was collected on the clean diamond under the same conditions. Raw spectra were pre-processed as follows (OPUS 7.5, Bruker Optics): correction for atmospheric carbon dioxide and water vapor (in order to remove the contribution of theses specimens to infrared spectra), vector normalization (in order to standardize spectra to the total absorbance), cut in the 1800–700 cm^{-1} range, and baseline correction (in order to minimize interference from baseline distortions, hence offering more reliable quantitative intensity measurements). The choice of using the fingerprint region (1800–700 cm^{-1}) was made according to literature, in particular considering previous studies and the macromolecules of interest within VH samples. Spectral profiles were analyzed both in absorbance and second derivative modes, with a focus on the height and the center position of specific peaks of interest.

2.3. Statistical analysis

A first exploratory analysis of spectral data was performed by means of Principal Component Analysis (PCA), which decomposes the pre-processed spectral data into a few numbers of PCs accountable for most of the variance (Eq. (1)):

$$\mathbf{X} = \mathbf{TP}^{\mathrm{T}} + \mathbf{E} \tag{1}$$

with **X** representing the pre-processed spectral data, **T** the PCA scores, **P** the loadings, and **E** the residuals [35–37]. Here, PCA was employed to assess the evolution of spectral profiles as a function of the post-mortem interval (PMI). The PCA toolbox for MATLAB was used [38].

Then, three supervised classification approaches were employed and compared: Partial Least Squares-Linear Discriminant Analysis (PLS-DA), K-Nearest neighbors (KNN), and Random Forest (RF), by means of the Classification toolbox for MATLAB and the PLS Toolbox 9.3.1, 2024, Eigenvector Research, Inc. [39]. To do this, the total dataset was automatically split into train and test sets (80 %–20 %, respectively), by means of the Onion algorithm (PLS Toolbox 9.3.1, 2024, Eigenvector Research, Inc.), which first selects a ring of the most unique samples that are used in the calibration set; then, a ring of less unique samples, inside the first set, is put into the validation set; this procedure is repeated two more times, letting obtain are three outer rings of most unique and less unique samples; finally, all remaining samples are randomly split into calibration and validation. Moreover, the algorithm was forced to keep the replicate spectra together in either the train or test sets. KNN is defined as a distance-based non-parametric classification method. First, a distance matrix – here Euclidean – was built analyzing all points in the data, then used to identify the K-closest neighbors, with K being the number of neighbors. The most common class for these K-closest data points was determined and, finally, the class of belonging of sample data determined [40]. Hence, the Euclidean distance between two objects $X_1 = (x_{11}, x_{12}, \cdots, x_{1n})$ and $X_2 = (x_{21}, x_{22}, \cdots, x_{2n})$ is measured:

$$dist(X_1, X_2) = \sqrt{\sum_{i=1}^{n} (x_{1i} - x_{2i})^2} \tag{2}$$

Then, the class of belonging of sample data (d) is determined, hence the model calculates the weight of d belonging to each class C_j as:

$$\mathrm{W(d, C_J)} = \sum_{i=1}^{k} sim(d_i, d) \diagup \left(d_i, C_j\right) \tag{3}$$

with $sim(d_i, d)$ being the similarity between d and the i^{th} nearest neighbor d_i [41]. Here, $K = 3$ was selected.

An RF-based classification algorithm was also employed. RF derives from the combination of CART (Classification And Regression Trees) and bootstrapping aggregation algorithms [42]. Briefly, RF combines predictive trees, which are built including a random selection of samples and variables [43]. A decision tree is produced, based on hierarchically-connected nodes that correspond to a variable value that carries the class information; then, a response, corresponding to a leaf (decision node) of the tree, is sought by recursively partitioning into branches and descending nodes [43]. At the end of this process, all the trees in the forest, comprise ~60 % of all samples, are trained and used to build the model, while the remaining samples (test sets) are employed to assess the classification accuracy [44]. Here, the model was built by employing 500 trees and 20 random variables.

PLS-DA is based on PLS regression (commented below) and relies on two fundamental equations:

$$\mathbf{X} = \mathbf{TP}^{T} + \mathbf{E} \tag{4}$$

$$\mathbf{Y} = \mathbf{TQ}^{T} + \mathbf{F} \tag{5}$$

with **X** representing the pre-processed spectral data, decomposed into P orthogonal scores **T** and loading matrix **P**, and with **Y** representing the response variable vector, decomposed into P orthogonal scores **T** and loading matrix **Q**; **E** and **F** are the error matrices. Once the weights matrix **W** is defined, **T** is:

$$\mathbf{T} = \mathbf{XW}\left(\mathbf{P}^{T}\mathbf{W}\right)^{-1} \tag{6}$$

Based on this, the PLS-DA algorithm lets calculate the regression coefficient $\widehat{\mathbf{B}}$ as:

$$\widehat{\mathbf{B}} = \mathbf{W}\left(\mathbf{P}^{T}\mathbf{W}\right)^{-1}\mathbf{Q}^{T} \tag{7}$$

from which a hypothetical unknown sample value of **Y** may be predicted: $\widehat{\mathbf{Y}} = \mathbf{X}\widehat{\mathbf{B}}$ [40].

Then, the PLS regression technique (PLSR) was employed to explore the spectral variability as a function of a systematic change occurring in samples (Regression toolbox for MATLAB) [45,46]. The algorithm details are the same as those explained above for PLS-DA. PLSR was employed since it allows for building predictive models correlating a spectral response to the target variable of interest.

The construction of models in both the classification and regression procedures was monitored by accurate selection of the number of latent variables/neighbors and by using metrics like root mean squared error of calibration (RMSEC) and of cross validation (RMSECV) and by cross validation (CV) procedures, specifically venetian blinds, where each test set is established by the selection of every i^{th} object in the dataset,

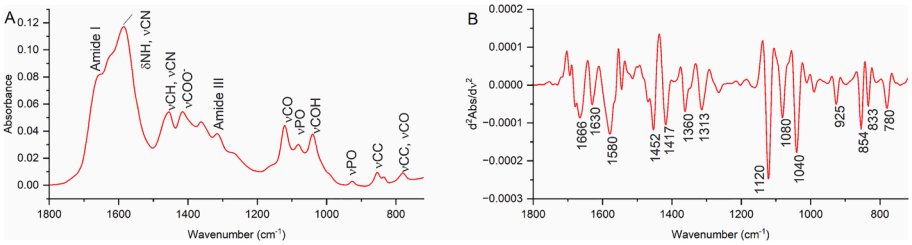

Fig. 1. Absorbance (A) and second derivative (B) spectral profiles of a representative VH sample in the 1800–700 cm^{-1} range.

Table 1
Centre position (wavenumbers, cm^{-1}), vibrational mode and biochemical assignment of the peaks identified in the VH representative absorbance spectrum in the 1800–700 cm^{-1} spectral range [AAs: amino acids; FAs: fatty acids] [2,31,50–55].

Wavenumber (cm^{-1})		Vibrational mode and biochemical assignment
Absorbance	Second derivative	
~1657	~1666	Amide I (ν C═O, C—N): α helices
	~1630	Amide I (ν C═O, C—N): β sheets, ν NH_3
~1586	~1580	δ N—H, ν C—N
~1454	~1452	ν C—H (mainly lipids) ν C—N (proteins and urea)
~1410	~1417	ν COO^- (free AAs, free FAs, hyaluronic acid)
~1314	~1313	Amide III (ν C—N, in-plane δ N—H)
~1120	~1120	ν C—O (lactate)
~1080	~1080	ν P—O
~1040	~1040	ν C—OH (glycogen and glucose)
~923	~925	ν P—O, ν C—O (DNA)
~851	~854	ν C—C (lactate)
~780	~780	ν C—O, ν C—C (carbohydrates)

starting with objects numbered 1 through *i* [47].

Finally, a variable selection procedure was performed by means of the Genetic Algorithm combined with PLS regression (GA-PLS). Variable selection aims at extracting key features, in this case key peaks, from the second derivative infrared spectra, to simplify the model and, hence, its predictive capabilities [48]. Briefly, considering spectra as the *X* data and the values to be predicted as the *Y* data, a random *X* subset can be selected, and the RMSECV is calculated by PLS regression and CV procedures: the iteration of this procedure by GA lets identify the variable subsets providing the lowest RMSECV (PLS Toolbox 9.3.1, 2024, Eigenvector Research, Inc.). In particular, (1) an initial population of variable sets was built (population size 64); (2) a PLSR model (4 LVs) was fit to each set, and a venetian blind-based CV (10 splits and bind, 1 iteration) was used to assess the performance; (3) the sets characterized by high performance were select to survive in the next "generation"; (4) new variable sets were generated by crossover of variables among the surviving sets and by "mutating" the selection/non-selection criterion for some single variables; (5) these new surviving and modified sets were fitted again going back to step (2) [49]. Here, the following parameters were used: population size 64, window width 4, initial terms 30 %, max generation 100, mutation rate 0.005.

2.4. Spectral analysis

Some spectral regions of particular interest were more deeply analyzed. The curve fitting procedure was performed on these regions upon local straight baseline correction and vector normalization. The number and position of the underlying subpeaks were identified by the analysis of second derivative minima and fixed during the fitting procedure by means of Gaussian functions (OriginPro 2023b, OriginLab Corporation).

Pre-processed spectra were fitted by means of a combination of Gaussian curves ($y = y_0 + \frac{A}{w\sqrt{\pi/2}} e^{-2\frac{(x-x_c)^2}{w}}$); the centre ($x_c$), the integrated area ($A$), and the width ($w$) of the main vibrational features identified by multivariate approaches were assessed with the aim of quantifying the spectral differences in VH samples induced by different PMI values.

3. Results and discussion

3.1. Analysis of VH spectral profile

The absorbance spectral profiles of VH samples were analyzed, to highlight their main features to be assigned to specific vibrational modes. In Fig. 1, for simplicity, the description of the profile of a VH sample collected at a PMI < 10 h, considered representative of the sample type, is reported. Table 1 reports the center position of the main infrared peaks identified by the analysis of second derivative minima. Assignments were attributed according to literature [2,31,50–55].

The spectral profile of human VH, besides being consistent with the one reported in literature for animal samples [2,31,32], also reflects its known composition. VH is mainly composed of water (*ca.* 90 %) and of solid fibrillary components, represented by glycosaminoglycans and collagen [56]. In particular, collagen, mostly consisting of type II collagen, has been reported at a concentration of 280–1360 μg/ml [57]. All glycosaminoglycans are combined with proteins to form proteoglycans, except for hyaluronic acid, the most abundant one, present at 140–340 μg/ml concentrations [58]. There are also non-collagenous proteins, like glycoproteins (i.e. opticin and fibrillin), and non-structural proteins, including immunoglobulins and complement proteins [56]. All these VH components are reflected by the infrared spectrum. Several peaks can be ascribed to proteins, like those at ~1657 cm^{-1} (Amide I), ~1586 cm^{-1} (NH and CN bonds), ~1410 cm^{-1} (COO^- moieties of free amino acids), and ~1314 cm^{-1} (Amide III). The sugar moieties typical of glycosaminoglycans and glycoproteins are also displayed by the infrared spectrum with the bands at ~1040 cm^{-1} (COH^- moieties), and ~850 cm^{-1} and ~780 cm^{-1} (CO and CC moieties). Moreover, some other compounds are known to be present in VH, and some of them are considered widely useful for post-mortem analyses. Among them, there is creatinine, generated by a non-enzymatic irreversible mechanism from creatine: its presence in VH has been reported in literature, and a correlation between its increase and PMI has been suggested [59]. The most prominent infrared band of creatine/creatinine is centered at ~1625 cm^{-1} [60,61]. Urea is also present in VH samples, but it is considered more stable in relation to PMI; its main absorption bands are centered at ~1625 cm^{-1} (δ NH_2), ~1590 cm^{-1} (ν CO), and ~1450 cm^{-1} (ν CN) [62]. Nucleic acids are also present in VH, as evidenced by the peaks at ~1080 cm^{-1} and ~925 cm^{-1}, and their decrease along with the increase of the PMI has been reported in literature [2]. Among carbohydrates, lactate is considered a crucial marker in VH: its concentration is 2.88–5.06 mmol/l in the VH of living humans, which significantly increase along with increasing PMI [59]. The main spectral features ascribable to this molecule are centered at ~1120 cm^{-1} (C—O moieties) and ~855 cm^{-1} (CO and CC moieties).

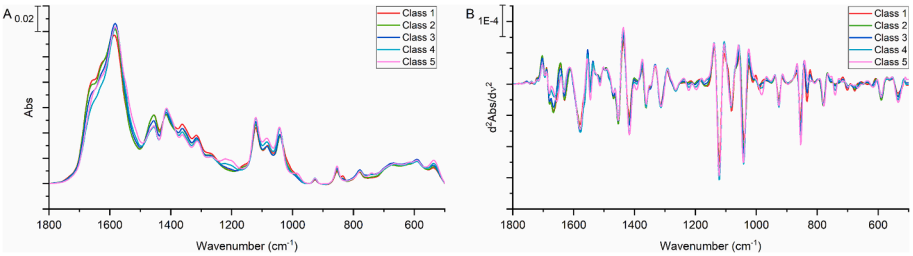

Fig. 2. Average absorbance (A) and second derivative (B) spectral profile of a representative VH sample from Classes 1–5, in the 1800–700 cm^{-1} range.

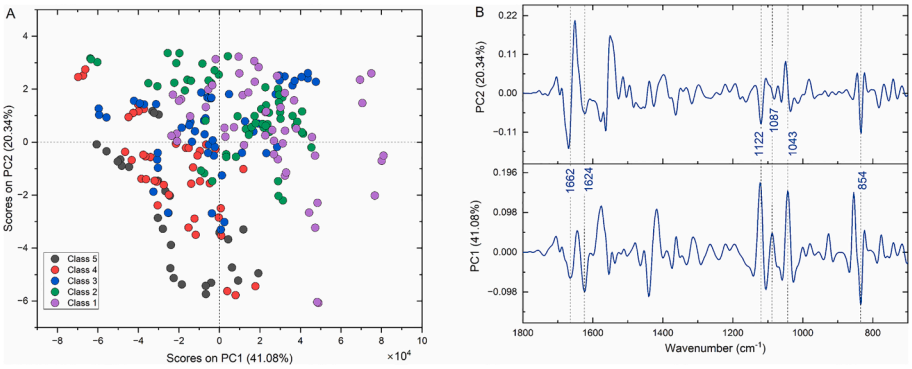

Fig. 3. (A) PCA scores plot calculated on the ATR-FTIR spectra of Classes 1–5 (1800–700 cm^{-1} range) and (B) corresponding loading spectra.

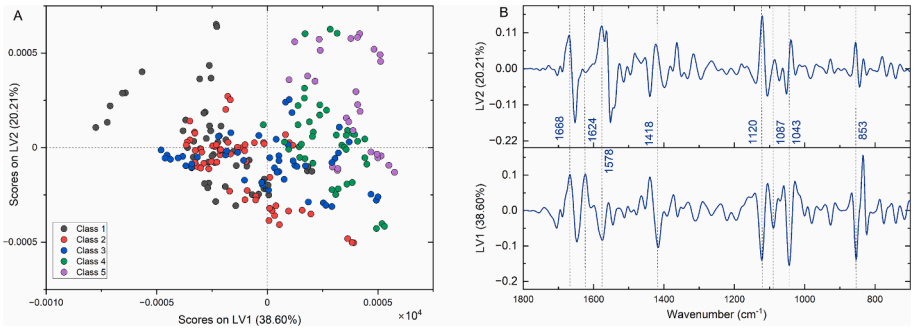

Fig. 4. (A) PLS-DA scores plot calculated on ATR-FTIR spectra of Classes 1–5 (1800–700 cm^{-1} range) and (B) corresponding loading spectra.

3.2. Statistical analyses and machine learning

For PCA and classification procedures, VH samples were divided into N. 5 classes, according to the PMI: Class 1 < 10.00 h; Class 2 = 10.33–20.00 h; Class 3 = 20.83–40.00 h; Class 4 = 41.00–80.00 h; Class 5 > 81.00. Fig. 2 displays the average absorbance and second derivative spectral profiles of VH samples of Classes 1–5 in the 1800–700 cm^{-1} range.

As previously described, PCA was first exploited as an exploratory analysis of second derivative spectral data (pre-processing: mean centering; 4 PCs; Fig. 3). The PCA scores plot evidenced a localization of scores consistent with the class division: a relatively good segregation between Class 1 and Classes 4 and 5 was found, while Class 1 appears almost superimposable with Classes 2 and 3. These results are not unexpected since spectral changes are mainly ascribable to PMI degradation processes, but they can also derive from other biological mechanisms which cannot be verified. Although not sharp, this evidence is suggests the real possibility of exploiting this approach for a reliable PMI evaluation. The PC1 loading displayed as the most discriminant spectral features the peaks centered at ~1662 cm^{-1} (Amide I – α helices), ~1624 cm^{-1} (Amide I – β sheets; creatinine and urea), ~1122 cm^{-1} (carbohydrates – lactate), 1087 cm^{-1} (phosphate groups), ~1043 cm^{-1} (carbohydrates), and ~854 cm^{-1} (carbohydrates – lactate). These results suggested that the main modifications due to increasing PMI are related to changes of proteins, carbohydrates, and nitrogen-containing compounds, such as urea.

After exploration of data with PCA, three different supervised classification techniques were employed, to systematically classify samples. First, PLS-DA was used on second derivative VH spectra (pre-processing: mean centering; 3 latent variables – LVs; CV: venetian blinds w/ 10 splits and blind). Fig. 4 reports the scores on LV1 and LV2 and the corresponding loading spectra: also in this case, a relatively good segregation between Class 1 and Classes 4 and 5 was found, while Class 1 appears almost superimposable with Classes 2 and 3. Interestingly, also the spectral loadings corresponding to LV1 and LV2 reflected the same molecular modifications induced on VH by the increasing PMI, mainly regarding proteins, carbohydrates, and nitrogen-containing compounds: ~1662 cm^{-1} (Amide I – α helices), ~1624 cm^{-1} (Amide I – β sheets; creatinine and urea), ~1578 cm^{-1} (proteins), ~1418 cm^{-1} (free AAs, free FAs, and hyaluronic acid), ~1120 cm^{-1} (carbohydrates – lactate), ~1087 cm^{-1} (phosphate groups), ~1043 cm^{-1} (carbohydrates), and ~853 cm^{-1} (carbohydrates – lactate).

The validation of the classification model was assessed by calculation of sensitivity, specificity, classification error, and precision together

Table 2
Model accuracy assessment for PLS-DA (3 LVs), KNN (K = 3), and RF (500 trees). Accuracy was assessed by the analysis of sensitivity, specificity, classification error, and precision, before and after cross validation. RMSEC, RMSEP, and RMSECV were also calculated for PLS-DA.

PLSDA Classification

MODEL RESULTS

Confusion Matrix:

Class:	TP	FP	TN	FN	N	F1	SENS	SPEC	CLASS.ERR.	PREC	RMSEC
Class 1	0.489	0.091	0.908	0.511	45	0.550	0.756	0.810	0.217	0.843	0.340
Class 2	0.786	0.324	0.676	0.214	42	0.541	0.857	0.517	0.313	0.708	0.394
Class 3	0.187	0.072	0.928	0.812	48	0.269	0.875	0.353	0.386	0.722	0.427
Class 4	0.571	0.566	0.943	0.429	28	0.604	0.929	0.748	0.161	0.502	0.327
Class 5	0.875	0.043	0.957	0.125	24	0.808	1.000	0.902	0.049	0.953	0.254

Confusion Table:

	Actual Class				
	Class 1	Class 2	Class 3	Class 4	Class 5
Predicted as Class 1	22	7	6	0	0
Predicted as Class 2	20	33	27	0	0
Predicted as Class 3	3	2	9	5	1
Predicted as Class 4	0	0	6	16	3
Predicted as Class 5	0	0	0	7	21
Predicted as Unass.	0	0	0	0	0

CV RESULTS

Confusion Matrix (CV):

Class:	TP	FP	TN	FN	N	F1	SENS	SPEC	CLASS.ERR.	PREC	RMSECV
Class 1	0.467	0.134	0.867	0.533	45	0.494	0.711	0.782	0.253	0.777	0.353
Class 2	0.667	0.310	0.690	0.333	42	0.487	0.833	0.524	0.321	0.683	0.399
Class 3	0.187	0.050	0.950	0.812	48	0.281	0.854	0.403	0.371	0.789	0.433
Class 4	0.607	0.088	0.912	0.393	28	0.576	0.893	0.717	0.195	0.873	0.332
Class 5	0.833	0.043	0.957	0.167	24	0.784	1.000	0.902	0.049	0.951	0.258

Confusion Table (CV):

	Actual Class				
	Class 1	Class 2	Class 3	Class 4	Class 5
Predicted as Class 1	21	11	8	0	0
Predicted as Class 2	21	28	24	0	0
Predicted as Class 3	3	0	9	4	1
Predicted as Class 4	0	3	7	17	4
Predicted as Class 5	0	0	0	7	20
Predicted as Unass.	0	0	0	0	0

PREDICTION RESULTS

Confusion Matrix (PRED):

Class:	TP	FP	TN	FN	N	F1	SENS	SPEC	CLASS.ERR.	PREC	RMSEP
Class 1	0.500	0.081	0.919	0.500	6	0.500	0.500	0.838	0.331	0.860	0.329
Class 2	0.733	0.143	0.857	0.267	15	0.733	0.800	0.571	0.314	0.837	0.437
Class 3	0.333	0.027	0.973	0.667	6	0.444	1.000	0.351	0.324	0.925	0.378
Class 4	1.000	0.100	0.900	0.000	13	0.896	1.000	0.767	0.117	0.909	0.425
Class 5	1.000	0.000	1.000	0.000	3	1.000	1.000	0.850	0.075	1.000	0.219

Confusion Table (PRED):

	Actual Class				
	Class 1	Class 2	Class 3	Class 4	Class 5
Predicted as Class 1	3	3	0	0	0
Predicted as Class 2	3	11	1	0	0
Predicted as Class 3	0	1	2	0	0
Predicted as Class 4	0	0	3	13	0
Predicted as Class 5	0	0	0	0	3
Predicted as Unass.	0	0	0	0	0

KNN Classification

MODEL RESULTS

Confusion Matrix:

Class:	TP	FP	TN	FN	N	F1	SENS	SPEC	CLASS.ERR.	PREC
Class 1	0.767	0.057	0.943	0.233	43	0.786	1.000	1.000	0.000	0.931
Class 2	0.733	0.086	0.914	0.267	45	0.733	1.000	1.000	0.000	0.895
Class 3	0.773	0.143	0.857	0.227	44	0.694	1.000	1.000	0.000	0.844
Class 4	0.606	0.053	0.947	0.394	33	0.656	1.000	1.000	0.000	0.919
Class 5	0.631	0.024	0.976	0.368	19	0.686	1.000	1.000	0.000	0.963

(*continued on next page*)

Table 2 (*continued*)

Confusion Table:

	Actual Class				
	Class 1	Class 2	Class 3	Class 4	Class 5
Predicted as Class 1	33	6	2	0	0
Predicted as Class 2	6	33	4	2	0
Predicted as Class 3	4	5	34	9	2
Predicted as Class 4	0	1	2	20	5
Predicted as Class 5	0	0	2	2	12
Predicted as Unass.	0	0	0	0	0

CV RESULTS

Confusion Matrix (CV):

Class:	TP	FP	TN	FN	N	F1	SENS	SPEC	CLASS.ERR.	PREC
Class 1	0.744	0.028	0.972	0.256	43	0.810	0.930	1.000	0.035	0.964
Class 2	0.778	0.086	0.914	0.222	45	0.761	0.911	0.971	0.059	0.900
Class 3	0.795	0.129	0.871	0.204	44	0.722	0.886	0.943	0.085	0.860
Class 4	0.697	0.053	0.947	0.303	33	0.719	0.818	0.960	0.111	0.929
Class 5	0.737	0.018	0.982	0.263	19	0.778	0.895	0.988	0.059	0.976

Confusion Table (CV):

	Actual Class				
	Class 1	Class 2	Class 3	Class 4	Class 5
Predicted as Class 1	32	4	0	0	0
Predicted as Class 2	6	35	6	0	0
Predicted as Class 3	5	5	35	8	0
Predicted as Class 4	0	1	2	23	5
Predicted as Class 5	0	0	1	2	14
Predicted as Unass.	0	0	0	0	0

PREDICTION RESULTS

Confusion Matrix (PRED):

Class:	TP	FP	TN	FN	N	F1	SENS	SPEC	CLASS.ERR.	PREC
Class 1	0.875	0.053	0.947	0.125	8	0.823	1.000	1.000	0.000	0.943
Class 2	0.667	0.000	1.000	0.333	12	0.800	1.000	1.000	0.000	1.000
Class 3	0.900	0.139	0.861	0.100	10	0.750	1.000	1.000	0.000	0.866
Class 4	0.750	0.053	0.947	0.250	8	0.750	1.000	1.000	0.000	0.934
Class 5	0.875	0.000	1.000	0.125	8	0.933	1.000	1.000	0.000	1.000

Confusion Table (PRED):

	Actual Class				
	Class 1	Class 2	Class 3	Class 4	Class 5
Predicted as Class 1	7	1	1	0	0
Predicted as Class 2	0	8	0	0	0
Predicted as Class 3	1	2	9	2	0
Predicted as Class 4	0	1	0	6	1
Predicted as Class 5	0	0	0	0	7
Predicted as Unass.	0	0	0	0	0

RF Classification

MODEL RESULTS

Confusion Matrix:

Class:	SENS	SPEC	CLASS.ERR	PREC
Class 1	1.000	0.990	0.005	0.980
Class 2	0.980	1.000	0.010	1.000
Class 3	1.000	0.990	0.005	0.980
Class 4	1.000	1.000	0.000	1.000
Class 5	1.000	1.000	0.000	1.000

Confusion Table:

	Actual Class				
	Class 1	Class 2	Class 3	Class 4	Class 5
Predicted as Class 1	40	0	1	0	0
Predicted as Class 2	1	44	0	0	0
Predicted as Class 3	0	0	45	0	0
Predicted as Class 4	0	0	1	32	0
Predicted as Class 5	0	0	0	0	21
Predicted as Unass.	0	0	0	0	0

(*continued on next page*)

Table 2 (*continued*)

CV RESULTS

Confusion Matrix (CV):

Class:	SENS	SPEC	CLASS.ERR	PREC
Class 1	0.800	0.980	0.110	0.910
Class 2	0.820	0.940	0.120	0.820
Class 3	0.890	0.930	0.090	0.800
Class 4	0.820	0.950	0.115	0.790
Class 5	0.810	0.980	0.105	0.850

Confusion Table (CV):

	Actual Class				
	Class 1	Class 2	Class 3	Class 4	Class 5
Predicted as Class 1	32	5	2	1	0
Predicted as Class 2	3	37	5	0	0
Predicted as Class 3	0	3	40	2	0
Predicted as Class 4	0	0	3	27	3
Predicted as Class 5	0	0	0	4	17
Predicted as Unass.	0	0	0	0	0

PRED RESULTS

Confusion Matrix (PRED):

Class:	SENS	SPEC	CLASS.ERR	PREC
Class 1	0.910	0.860	0.115	0.670
Class 2	0.500	0.820	0.34	0.500
Class 3	0.110	0.890	0.5	0.200
Class 4	0.630	0.920	0.225	0.630
Class 5	1.000	1.000	0.000	1.00

Confusion Table (PRED):

	Actual Class				
	Class 1	Class 2	Class 3	Class 4	Class 5
Predicted as Class 1	10	1	2	1	0
Predicted as Class 2	5	6	1	0	0
Predicted as Class 3	0	5	1	3	0
Predicted as Class 4	0	0	3	5	0
Predicted as Class 5	0	0	0	0	6
Predicted as Unass.	0	0	0	0	0

with the RMSEC, RMSECV, and RMSEP metrics, before and after venetian blinds CV, as follows:

$$RMSEC \Big/ RMSEP = \sqrt{\frac{\sum_{i=1}^{m} (y_i - \hat{y}_i)^2}{m}} \tag{8}$$

$$RMSECV = \sqrt{\frac{\sum_{j=1}^{J} \sum_{i=1}^{m_J} (y_i - \hat{y}_i)^2}{m_J}} \tag{9}$$

RMSEC/RMSEP is a measure of the fit to the model data, with i representing all m observations used to build the model, y_i the predicted value for I and $\hat{y}_i$ the true value for i; RMSECV estimates the predictive power on new data, with J representing the CV subsets and i the m_J samples in the CV subsets not used to build the model.

As regards sensitivity, specificity, classification error, and precision:

$$SENS = \frac{TP}{TP + FN} \tag{10}$$

$$SPEC = \frac{TN}{TN + FP} \tag{11}$$

$$CLASS.ERR. = 1 - \frac{SENS + SPEC}{2} \tag{12}$$

$$PREC = \frac{TP}{TP + FP} \tag{13}$$

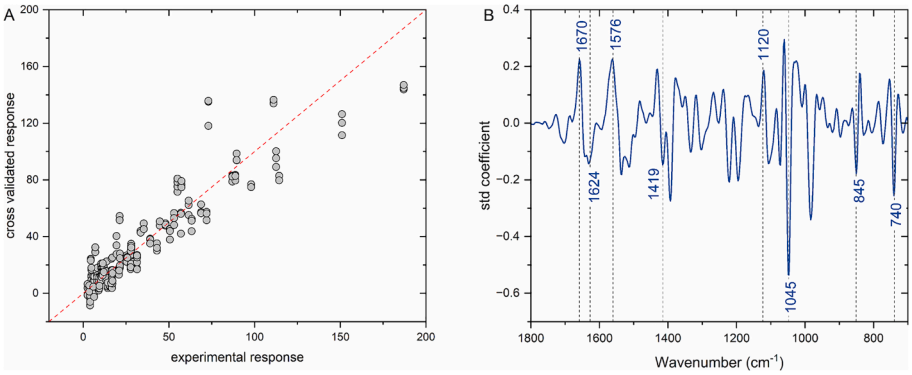

Fig. 5. (A) PLSR model calculated on ATR-FTIR spectra of Classes 1–5 (1800–700 cm^{-1} range) and (B) standardized regression coefficients.

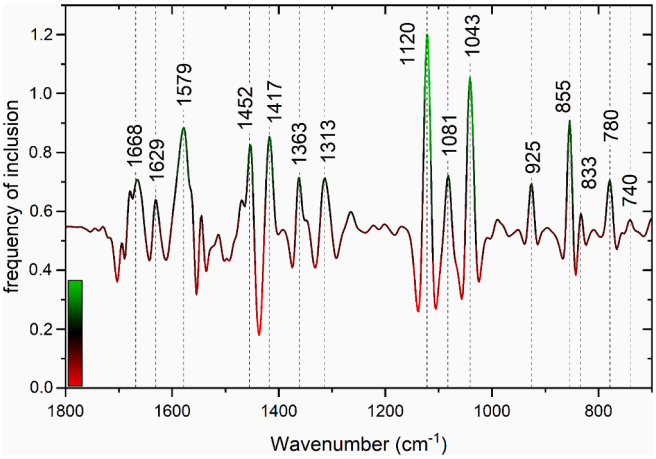

Fig. 6. Variable usage plot obtained by GA-PLSR variable selection procedure performed in the 1800–700 cm^{-1} range. The color scale indicates with green variables included with a high frequency.

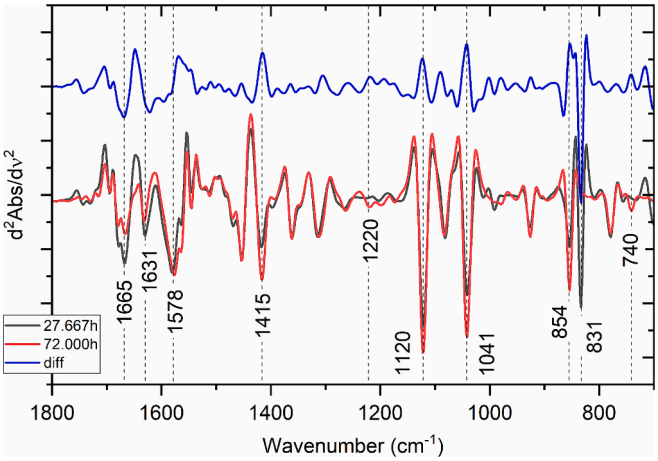

Fig. 7. Second derivative spectra (1800–700 cm^{-1} range) of the same VH sample collected after 27.67 h and after 72.00 h.

where TP is for true positives, FN is false negatives, TN is true negatives, and FP is false positives; here, classification error is calculated as the average of FP and FN rates for class.

Table 2 reports the validation results of the three classification models employed in this study, PLS-DA, KNN, and RF. Altogether, these results show a promising potential in the prediction of PMI from VH samples, which will be improved by the inclusion of a higher number of samples, both in the training and test sets.

PLSR was then employed to explore the spectral variability as a function of exact PMI values. The number of LVs was set at 4. Fig. 5 shows the PLSR model and the regression coefficient obtained from this analysis.

The PLSR model, obtained by plotting experimental responses vs cross validated predicted responses, showed a good correlation between spectral modifications and PMI. RMSEC was 11.457 and R^2 was 0.899; after CV, the accuracy of the model was given by RMSECV equal to 12.981 and R^2 to 0.878. The standardized regression coefficients, corresponding to the standardized x- and y-variables, were used to highlight the spectral changes related to the increasing PMI. The standardization of variables was performed by subtracting from them their sample mean and by dividing it by its standard deviation. All the spectral features changing in PCA and PLS-DA loadings appeared as the most prominent also in this analysis, including the bands at ~1670 cm^{-1} (Amide I – α helices), ~1624 cm^{-1} (Amide I – β sheets; creatinine and urea), ~1576 cm^{-1} (proteins), ~1419 cm^{-1} (free AAs, free FAs, and hyaluronic acid), and ~853 cm^{-1} (carbohydrates – lactate). Particularly relevant appeared the contribution of the bands centered at ~1120 cm^{-1} (carbohydrates – lactate) and ~1043 cm^{-1} (carbohydrates). In addition, a prominent contribution was also attributed to the peak centered at ~740 cm^{-1}, assigned to the δ C—H of tryptophan aromatic ring [63].

Finally, the Genetic Algorithm combined with PLS regression (GA-PLS) was exploited for variable selection. The result, displayed as variable usage plot (Fig. 6), confirmed what highlighted by the PLSR regression coefficients plot and provided a clearer view of the subset of variables that resulted to be the most relevant in the proposed regression model. First and foremost, carbohydrates appeared as the most important variables, as indicated by the peak centered at ~1043 cm^{-1} (glucose) and those at ~1120 cm^{-1} and ~855 cm^{-1} (lactate); a similar relevance was reported for the peaks centered at ~1452 cm^{-1} (here, mainly urea), ~1417 cm^{-1} (free AAs, free FAs, and hyaluronic acid), and ~1579 cm^{-1} (proteins).

To confirm the latter results, a profile comparison was performed between two infrared spectra obtained from the same VH sample, but collected at different PMIs, i.e. 27.67 h and 72.00 h. Fig. 7 displays the second derivative spectra, together with the difference spectrum. Clearly, most of the variables identified as the most important by the GA-PLSR procedure were also found by this simple comparison.

Altogether, the results obtained by the multivariate statistical approaches, besides confirming each other, are perfectly consistent with some of the known biochemical changes occurring in VH after death [2,10,31,32]. To more thoroughly investigate these modifications, the 1750–1500 cm^{-1}, 1300–950 cm^{-1}, and 950–720 cm^{-1} spectral ranges were more deeply investigated. The comparison of the fitting results obtained from Classes 1–5 is displayed in Fig. 8. The fitting parameters of interest within the three spectral ranges are reported in Table S3 (Supplementary Material). Area values for each fitted peak was compared among Classes 1–5, by a factorial analysis of variance (one-way ANOVA), followed by Tukey's multiple comparison test (Prism6, Graphpad Software, Inc. USA).

It is well known that proteins are degraded within tissues after death, following some crucial mechanisms, including for example the activity of proteases [64]: in particular, it has been reported that the ATP-independent calpain system is intensely triggered by the post-mortem increase of intracellular calcium, leading to a significant increase of proteolytic mechanisms [65]. This is confirmed by some spectral markers identified by the statistical procedures performed, which highlighted as among the most discriminant markers some bands assign to this macromolecule category. For example, the area of the bands centered at ~1660 cm^{-1} and ~1578 cm^{-1} respectively attributed to α-helix secondary structures and to proteins NH and CN bonds, decreases along with the increase of PMI: this could be related to the general protein degradation previously described. This is confirmed by the increase along increasing PMI of the integrated area of the band centered at ~1418 cm^{-1} (data not shown), assigned to free AAs, which is consistent with the proteolytic activity triggered post-mortem [65]. The band centered at ~1630 cm^{-1}, besides being generally attributed to β-sheet secondary structures of proteins [66], has also been reported to be attributable to creatine, creatinine, and urea [60,61]: creatine derives from the metabolism of some AAs, creatinine from the non-enzymatic transformation of creatine, while urea is obtained by transformation of the ammonia generated by the removal of the α-amino group in protein catabolism [59]. In other studies, a good correlation was found between PMI and creatine and creatinine levels in VH [67,68], while urea has been reported to be more stable along PMI [59]. The reported results are in accordance with this information, since a clear increase of the ~1630 cm^{-1} band as a function of increasing PMI was found. Finally, a peculiar behavior was reported for the band centered at ~740 cm^{-1} which was absent in Classes 1–3 and appeared in Class 4, doubling its values in Class 5. This band can be assigned to the tryptophan (Trp) amino acid

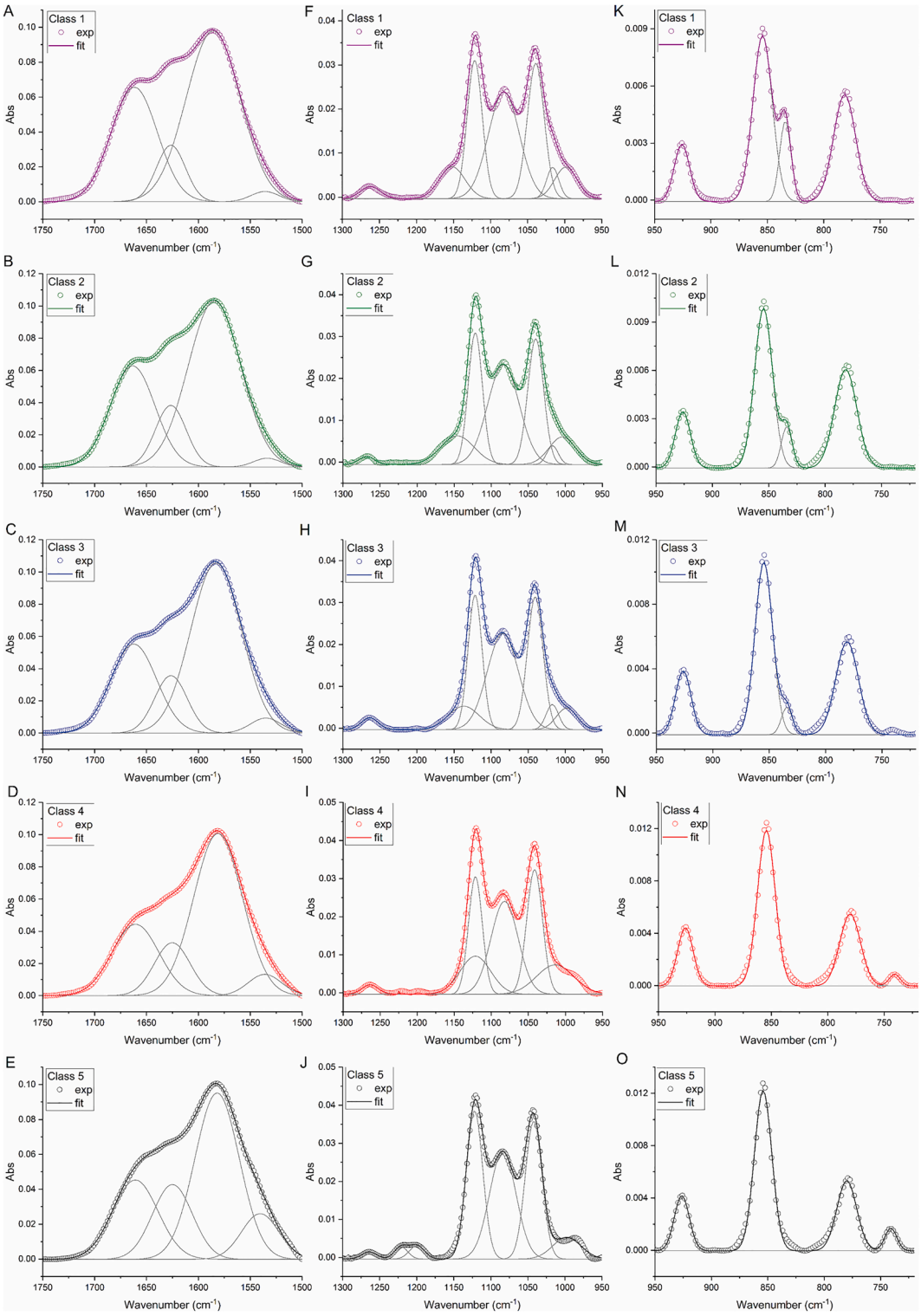

Fig. 8. Details of the curve fitting results in the 1750–1500 cm^{-1} (A–E), 1300–950 cm^{-1} (F–J), and 950–720 cm^{-1} (K–O) spectral ranges for Classes 1–5 (each row represents a class). The experimental spectra (empty dots) were deconvoluted by means of Gaussian functions (grey curves) obtaining the fitting curve (continuous thick lines).

[63], which was found to be highly statistically correlated with PMI and for this reason has been suggested as a useful tool to be taken into account in uncertain PMI cases [59,69]. Considering this interpretation, our findings are perfectly consistent with literature.

Carbohydrates seemed to play a crucial role in discriminating infrared spectra from VH samples at different PMIs. It is known that glucose is present in VH and that it slowly decreases over short PMIs; then, its levels are reported to remain stable for days and are coupled with an increase in lactate concentration [59,70]. The most peculiar infrared bands of glucose are reported to be centered at ~1035 cm^{-1} and ~835^{-1} [71,72]: both these bands were found as discriminant in the statistical procedures performed in this work, and the fitting analysis showed no change for the first and a strong decrease for the latter, which completely disappeared in Classes 4 and 5. As previously mentioned,

lactate is known to increase in VH along with increasing PMI: after death, given the oxygen absence, anaerobic glycolysis takes action, and the obtained pyruvate is converted into lactic acid [59,73]; after lactic acid increases in tissues post mortem, it can enter VH, due to the loss of function of the haemato-retinal barrier [59]. Infrared spectroscopy results confirmed this information, since in all the statistical procedures, the lactate-related bands were among the most prominent. In this light, the band centered at ~1120 cm^{-1}, considered as the most specific for this compound [71], after remaining constant in Classes 1–3, increased in Classes 4 and 5; more notably, another lactate-related band, at ~1220 cm^{-1}, was only present in Classes 4 and 5, with the latter showing an increase of one order of magnitude. The band at ~780 cm^{-1} is assigned more generally to carbohydrates, hence the absence of an increasing or decreasing trend may be due to the contribution of different species of compounds, including both glucose and lactate, together with other glycosylated compounds.

Finally, the band centered at ~1080 cm^{-1} appeared as relevant in the discrimination of VH samples at different PMIs: it is attributed to nucleic acids and the curve fitting procedure evidenced a slight decrease. This result is consistent with the literature and may suggest a process of fragmentation of nucleic acids within VH [2,31].

4. Conclusions

The present work reports the development of a new analytical approach based on ATR-FTIR spectroscopy coupled with multivariate statistical and machine learning procedures for assessing post-mortem interval from vitreous humor. This is the first time that a similar methodology has been applied on human samples for PMI assessment. Vitreous humor is a very promising biological matrix; in fact, given its isolated nature, which preserves it from contamination and delays decomposition respect to other fluids and tissues, VH is very useful in PMI evaluations during criminal investigations. Respect to other widely employed biological matrices, like bone, PMI appears very useful in the determination of short PMIs.

Several endogenous compounds are reported to be useful in this analysis, but the advantage of using ATR-FTIR stands in its label-free nature, which allows for the determination with one acquisition, at the same time, and on the same sample, of more than one compound. In fact, here our results display simultaneous mechanisms as relevant when PMI progresses, such as protein degradation and lactate formation. In this light, the present study strengthens the potentialities of ATR-FTIR coupled with chemometrics and machine learning to study human biofluids for several purposes. Moreover, this research represents a solid proof of concept for the use of this approach for assessing PMI in forensic investigations, which in the future will be strengthened by including a higher number of samples and by taking into account a wider variety of causes of death, with the final aim of creating a big reliable dataset of infrared spectra to be computationally compared with unknown ones.

CRediT authorship contribution statement

Valentina Notarstefano: Conceptualization, Data curation, Formal analysis, Investigation, Methodology, Validation, Visualization, Writing – original draft, Writing – review & editing. **Chiara Santoni:** Data curation, Formal analysis, Investigation, Methodology, Writing – original draft, Writing – review & editing. **Eva Montanari:** Conceptualization, Methodology, Supervision, Resources, Writing – original draft, Writing – review & editing. **Francesco Paolo Busardò:** Data curation, Methodology, Writing – review & editing. **Angelo Montana:** Data curation, Methodology, Writing – review & editing. **Giulia Orilisi:** Data curation, Formal analysis, Writing – review & editing. **Paolo Mariani:** Data curation, Resources, Writing – review & editing. **Elisabetta Giorgini:** Conceptualization, Supervision, Methodology, Resources, Writing – original draft, Writing – review & editing.

Declaration of competing interest

The authors declare that they have no known competing financial interests or personal relationships that could have appeared to influence the work reported in this paper.

Acknowledgment

We thank Dr. Eva Santolini for her precious contribution in the acquisition of ATR-FTIR spectra.

V.N. and P.M. acknowledge the received funding from the project Vitality – Project Code ECS00000041, CUP I33C22001330007 - funded under the National Recovery and Resilience Plan (NRRP), Mission 4 Component 2 Investment 1.5 - 'Creation and strengthening of innovation ecosystems,' construction of 'territorial leaders in R&D' – Innovation Ecosystems - Project 'Innovation, digitalization and sustainability for the diffused economy in Central Italy – VITALITY' Call for tender No. 3277 of 30/12/2021, and Concession Decree No. 0001057.23-06-2022 of Italian Ministry of University funded by the European Union – NextGenerationEU.

Appendix A. Supplementary material

Supplementary data to this article can be found online at https://doi.org/10.1016/j.saa.2024.125326.

Data availability

Data will be made available on request.

References

[1] A. Mathur, Y.K. Agrawal, An overview of methods used for estimation of time since death, Aust. J. Forensic Sci. 43 (2011) 275–285, https://doi.org/10.1080/00450618.2011.568970.
[2] J. Zhang, X. Wei, J. Huang, H. Lin, K. Deng, Z. Li, Y. Shao, D. Zou, Y. Chen, P. Huang, Z. Wang, Attenuated total reflectance Fourier transform infrared (ATR-FTIR) spectral prediction of postmortem interval from vitreous humor samples, Anal. Bioanal. Chem. 410 (2018) 7611–7620, https://doi.org/10.1007/s00216-018-1367-1.
[3] B. Madea, Methods for determining time of death, Forensic Sci. Med. Pathol. 12 (2016) 451–485, https://doi.org/10.1007/s12024-016-9776-y.
[4] J. Hayman, M. Oxenham, Human Body Decomposition, Elsevier, 2016 doi: 10.1016/C2015-0-00038-7.
[5] M.J. Baker, J. Trevisan, P. Bassan, R. Bhargava, H.J. Butler, K.M. Dorling, P. R. Fielden, S.W. Fogarty, N.J. Fullwood, K.A. Heys, C. Hughes, P. Lasch, P. L. Martin-Hirsch, B. Obinaju, G.D. Sockalingum, J. Sulé-Suso, R.J. Strong, M. J. Walsh, B.R. Wood, P. Gardner, F.L. Martin, Using Fourier transform IR spectroscopy to analyze biological materials, Nat. Protoc. 9 (2014) 1771–1791, https://doi.org/10.1038/nprot.2014.110.
[6] E. Mistek, I.K. Lednev, Identification of species' blood by attenuated total reflection (ATR) Fourier transform infrared (FT-IR) spectroscopy, Anal. Bioanal. Chem. 407 (2015) 7435–7442, https://doi.org/10.1007/s00216-015-8909-6.
[7] K.M. Elkins, Rapid presumptive "Fingerprinting" of body fluids and materials by ATR FT-IR spectroscopy, J. Forensic Sci. 56 (2011) 1580–1587, https://doi.org/10.1111/j.1556-4029.2011.01870.x.
[8] S. Giuliano, E. Mistek-Morabito, I.K. Lednev, Forensic phenotype profiling based on the attenuated total reflection Fourier transform-infrared spectroscopy of blood: chronological age of the donor, ACS Omega 5 (2020) 27026–27031, https://doi.org/10.1021/acsomega.0c01914.
[9] A. Takamura, K. Watanabe, T. Akutsu, T. Ozawa, Soft and robust identification of body fluid using Fourier transform infrared spectroscopy and chemometric strategies for forensic analysis, Sci. Rep. 8 (2018) 8459, https://doi.org/10.1038/s41598-018-26873-9.
[10] A. Wójtowicz, A. Mitura, R. Wietecha-Posłuszny, R. Kurczab, M. Zawadzki, Spectroscopy as a useful tool for the identification of changes with time in post-mortem vitreous humor for forensic toxicology purposes, Monatsh. Chem. 152 (2021) 745–755, https://doi.org/10.1007/s00706-021-02786-8.
[11] L. Wang, H. Lin, Y. Luo, Q. Sun, Z. Li, Y. Chen, P. Huang, Z. Wang, J. Sun, Y. Tuo, Post-mortem interval estimation in rat liver tissues using attenuated total reflection Fourier transform infrared spectroscopy combined with chemometrics, Aust. J. Forensic Sci. 51 (2019) 527–537, https://doi.org/10.1080/00450618.2018.1429016.
[12] K. Yu, H. Zhang, Y. Liu, H. Wu, W. Cai, X. Wei, R. Liu, G. Wang, Q. Sun, Z. Wang, Adipose tissue estimates the postmortem interval based on ATR-FTIR spectroscopy,

Microchem. J. 164 (2021) 105977, https://doi.org/10.1016/j.microc.2021.105977.
[13] J. Zhang, B. Li, Q. Wang, C. Li, Y. Zhang, H. Lin, Z. Wang, Characterization of postmortem biochemical changes in rabbit plasma using ATR-FTIR combined with chemometrics: a preliminary study, Spectrochim. Acta A: Mol. Biomol. Spectrosc. 173 (2017) 733–739, https://doi.org/10.1016/j.saa.2016.10.041.
[14] J. Zhang, B. Li, Q. Wang, X. Wei, W. Feng, Y. Chen, P. Huang, Z. Wang, Application of Fourier transform infrared spectroscopy with chemometrics on postmortem interval estimation based on pericardial fluids, Sci. Rep. 7 (2017) 18013, https://doi.org/10.1038/s41598-017-18228-7.
[15] Z. Li, J. Huang, Z. Wang, J. Zhang, P. Huang, An investigation on annular cartilage samples for post-mortem interval estimation using Fourier transform infrared spectroscopy, Forensic Sci. Med. Pathol. 15 (2019) 521–527, https://doi.org/10.1007/s12024-019-00146-x.
[16] A. Baptista, M. Pedrosa, F. Curate, M.T. Ferreira, M.P.M. Marques, Estimation of the post-mortem interval in human bones by infrared spectroscopy, Int. J. Leg. Med. 136 (2022) 309–317, https://doi.org/10.1007/s00414-021-02641-9.
[17] V. Notarstefano, G. Gioacchini, H.J. Byrne, C. Zacà, E. Sereni, L. Vaccari, A. Borini, O. Carnevali, E. Giorgini, Vibrational characterization of granulosa cells from patients affected by unilateral ovarian endometriosis: new insights from infrared and Raman microspectroscopy, Spectrochim. Acta A: Mol. Biomol. Spectrosc. 212 (2019) 206–214, https://doi.org/10.1016/j.saa.2018.12.054.
[18] V.-M. Schmidt, P. Zelger, C. Wöss, M. Fodor, T. Hautz, S. Schneeberger, C.W. Huck, R. Arora, A. Brunner, B. Zelger, M. Schirmer, J.D. Pallua, Handheld hyperspectral imaging as a tool for the post-mortem interval estimation of human skeletal remains, Heliyon 10 (2024) e25844, https://doi.org/10.1016/j.heliyon.2024.e25844.
[19] V.M. Schmidt, P. Zelger, C. Wöss, C.W. Huck, R. Arora, E. Bechtel, A. Stahl, A. Brunner, B. Zelger, M. Schirmer, W. Rabl, J.D. Pallua, Post-mortem interval of human skeletal remains estimated with handheld NIR spectrometry, Biology 11 (2022) 1020, https://doi.org/10.3390/biology11071020.
[20] C. Woess, S.H. Unterberger, C. Roider, M. Ritsch-Marte, N. Pemberger, J. Cemper-Kiesslich, P. Hatzer-Grubwieser, W. Parson, J.D. Pallua, Assessing various Infrared (IR) microscopic imaging techniques for post-mortem interval evaluation of human skeletal remains, PLoS One 12 (2017) e0174552, https://doi.org/10.1371/journal.pone.0174552.
[21] R. Lindtner, A. Wurm, K. Kugel, J. Kühn, D. Putzer, R. Arora, D.C. Coraça-Huber, P. Zelger, M. Schirmer, J. Badzoka, C. Kappacher, C.W. Huck, J.D. Pallua, Comparison of mid-infrared handheld and benchtop spectrometers to detect Staphylococcus epidermidis in bone grafts, Bioengineering 10 (2023) 1018, https://doi.org/10.3390/bioengineering10091018.
[22] S. Longato, C. Wöss, P. Hatzer-Grubwieser, C. Bauer, W. Parson, S.H. Unterberger, V. Kuhn, N. Pemberger, A.K. Pallua, W. Recheis, R. Lackner, R. Stalder, J.D. Pallua, Post-mortem interval estimation of human skeletal remains by micro-computed tomography, mid-infrared microscopic imaging and energy dispersive X-ray mapping, Anal. Methods 7 (2015) 2917–2927, https://doi.org/10.1039/C4AY02943G.
[23] V.-M. Schmidt, P. Zelger, C. Woess, A.K. Pallua, R. Arora, G. Degenhart, A. Brunner, B. Zelger, M. Schirmer, W. Rabl, J.D. Pallua, Application of micro-computed tomography for the estimation of the post-mortem interval of human skeletal remains, Biology 11 (2022) 1105, https://doi.org/10.3390/biology11081105.
[24] L. Franceschetti, A. Amadasi, V. Bugelli, G. Bolsi, M. Tsokos, Estimation of late postmortem interval: where do we stand? A literature review, Biology 12 (2023) 783, https://doi.org/10.3390/biology12060783.
[25] T.V. Chirila, Y. Hong, Chapter C2 The vitreous humor, in: W. Murphy, J. Black, G. Hastings (Eds.), Handbook of Biomaterial Properties, Springer New York, New York, NY, 2016, pp. 125–134, https://doi.org/10.1007/978-1-4939-3305-1_12.
[26] R.A. James, P.A. Hoadley, B.G. Sampson, Determination of postmortem interval by sampling vitreous humour, Am. J. Forensic Med. Pathol. 18 (1997) 158–162, https://doi.org/10.1097/00000433-199706000-00010.
[27] P.N. Bishop, Structural macromolecules and supramolecular organisation of the vitreous gel, Prog. Retin. Eye Res. 19 (2000) 323–344, https://doi.org/10.1016/S1350-9462(99)00016-6.
[28] J. Sebag, Macromolecular structure of the corpus vitreus, Prog. Polym. Sci. 23 (1998) 415–446, https://doi.org/10.1016/S0079-6700(97)00035-X.
[29] R. Sharma, A.R. Diksha, B.K.B. Bhute, Application of artificial intelligence and machine learning technology for the prediction of postmortem interval: a systematic review of preclinical and clinical studies, Forensic Sci. Int. 340 (2022) 111473, https://doi.org/10.1016/j.forsciint.2022.111473.
[30] B.N. Kalra, Vitreous humor: a short review on post-mortem applications, J. Clin. Exp. Pathol. 05 (2015), https://doi.org/10.4172/2161-0681.1000199.
[31] K. Zhang, Q. Wang, R. Liu, X. Wei, Z. Li, S. Fan, Z. Wang, Evaluating the effects of causes of death on postmortem interval estimation by ATR-FTIR spectroscopy, Int. J. Leg. Med. 134 (2020) 565–574, https://doi.org/10.1007/s00414-019-02042-z.
[32] Z. Zhang, H. Lin, Z. Li, Y. Luo, L. Wang, L. Chen, P. Huang, Identification of fatal hypothermia via attenuated total reflection Fourier transform infrared spectroscopy of rabbit vitreous humour, Aust. J. Forensic Sci. 53 (2021) 27–39, https://doi.org/10.1080/00450618.2019.1629021.
[33] J. Sebag, S. Nie, K. Reiser, M.A. Charles, N.T. Yu, Raman spectroscopy of human vitreous in proliferative diabetic retinopathy, Invest. Ophthalmol. Vis. Sci. 35 (1994) 2976–2980.
[34] E.E. Rossi, A.L.B. Pinheiro, O.C. Baltatu, M.T.T. Pacheco, L. Silveira, Differential diagnosis between experimental endophthalmitis and uveitis in vitreous with Raman spectroscopy and principal components analysis, J. Photochem. Photobiol. B Biol. 107 (2012) 73–78, https://doi.org/10.1016/j.jphotobiol.2011.12.001.
[35] C.L.M. Morais, K.M.G. Lima, M. Singh, F.L. Martin, Tutorial: multivariate classification for vibrational spectroscopy in biological samples, Nat. Protoc. 15 (2020) 2143–2162, https://doi.org/10.1038/s41596-020-0322-8.
[36] F. Bonnier, H.J. Byrne, Understanding the molecular information contained in principal component analysis of vibrational spectra of biological systems, Analyst 137 (2012) 322–332, https://doi.org/10.1039/C1AN15821J.
[37] V. Notarstefano, A. Belloni, P. Mariani, G. Orilisi, G. Orsini, E. Giorgini, H.J. Byrne, Multivariate curve resolution-alternating least squares coupled with Raman microspectroscopy: new insights into the kinetic response of primary oral squamous carcinoma cells to cisplatin, Analyst 148 (2023), https://doi.org/10.1039/D3AN01182H.
[38] D. Ballabio, A MATLAB toolbox for Principal Component Analysis and unsupervised exploration of data structure, Chemom. Intel. Lab. Syst. 149 (2015) 1–9, https://doi.org/10.1016/j.chemolab.2015.10.003.
[39] D. Ballabio, V. Consonni, Classification tools in chemistry. Part 1: linear models. PLS-DA, Anal. Methods 5 (2013) 3790, https://doi.org/10.1039/c3ay40582f.
[40] M. Fordellone, A. Bellincontro, F. Mencarelli, Partial least squares discriminant analysis: a dimensionality reduction method to classify hyperspectral data, Stat. Appl. – Ital. J. Appl. Stat. 31 (2020) 181–200, https://doi.org/10.26398/IJAS.0031-010.
[41] R. Li, S. Li, Multimedia image data analysis based on KNN algorithm, Comput. Intell. Neurosci. 2022 (2022) 1–8, https://doi.org/10.1155/2022/7963603.
[42] L. Breiman, Random Forests, Mach. Learn. 45 (2001) 5–32, https://doi.org/10.1023/A:1010933404324.
[43] B.P.O. Lovatti, M.H.C. Nascimento, Á.C. Neto, E.V.R. Castro, P.R. Filgueiras, Use of Random forest in the identification of important variables, Microchem. J. 145 (2019) 1129–1134, https://doi.org/10.1016/j.microc.2018.12.028.
[44] P.S. Gromski, H. Muhamadali, D.I. Ellis, Y. Xu, E. Correa, M.L. Turner, R. Goodacre, A tutorial review: metabolomics and partial least squares-discriminant analysis – a marriage of convenience or a shotgun wedding, Anal. Chim. Acta 879 (2015) 10–23, https://doi.org/10.1016/j.aca.2015.02.012.
[45] M.E. Keating, H. Nawaz, F. Bonnier, H.J. Byrne, Multivariate statistical methodologies applied in biomedical Raman spectroscopy: assessing the validity of partial least squares regression using simulated model datasets, Analyst 140 (2015) 2482–2492, https://doi.org/10.1039/C4AN02167C.
[46] V. Consonni, G. Baccolo, F. Gosetti, R. Todeschini, D. Ballabio, A MATLAB toolbox for multivariate regression coupled with variable selection, Chemom. Intel. Lab. Syst. 213 (2021) 104313, https://doi.org/10.1016/j.chemolab.2021.104313.
[47] E. Lopez, J. Etxebarria-Elezgarai, J.M. Amigo, A. Seifert, The importance of choosing a proper validation strategy in predictive models. A tutorial with real examples, Anal. Chim. Acta 1275 (2023) 341532, https://doi.org/10.1016/j.aca.2023.341532.
[48] G. Gioacchini, V. Notarstefano, E. Sereni, C. Zacà, G. Coticchio, E. Giorgini, L. Vaccari, O. Carnevali, A. Borini, Does the molecular and metabolic profile of human granulosa cells correlate with oocyte fate? New insights by Fourier transform infrared microspectroscopy analysis, in: MHR: Basic Science of Reproductive Medicine, 2018, https://doi.org/10.1093/molehr/gay035.
[49] T. Mehmood, K.H. Liland, L. Snipen, S. Sæbø, A review of variable selection methods in Partial Least Squares Regression, Chemom. Intel. Lab. Syst. 118 (2012) 62–69, https://doi.org/10.1016/j.chemolab.2012.07.010.
[50] Y. Nishikawa, K. Fujiwara, M. Osawa, K. Takamura, Trace analysis of human skin secretions by surface-enhanced infrared spectroscopy: detection of lactate, Anal. Sci. 9 (1993) 811–815, https://doi.org/10.2116/analsci.9.811.
[51] A.C.S. Talari, M.A.G. Martinez, Z. Movasaghi, S. Rehman, I.U. Rehman, Advances in Fourier transform infrared (FTIR) spectroscopy of biological tissues, Appl. Spectrosc. Rev. 52 (2017) 456–506, https://doi.org/10.1080/05704928.2016.1230863.
[52] T. Ube, K. Yamamoto, T. Ishiguro, Transmission infrared micro-spectroscopic study of lactic acid production in cultured cells, Vib. Spectrosc. 98 (2018) 8–14, https://doi.org/10.1016/j.vibspec.2018.06.012.
[53] V. Notarstefano, G. Gioacchini, E. Giorgini, N. Montik, A. Ciavattini, A.R. Polidori, F.A. Candela, L. Vaccari, M. Cignitti, O. Carnevali, The impact of controlled ovarian stimulation hormones on the metabolic state and endocannabinoid system of human cumulus cells, IJMS 21 (2020) 7124, https://doi.org/10.3390/ijms21197124.
[54] V. Notarstefano, A. Belloni, S. Sabbatini, C. Pro, G. Orilisi, R. Monterubbianesi, V. Tosco, H.J. Byrne, L. Vaccari, E. Giorgini, Cytotoxic effects of 5-azacytidine on primary tumour cells and cancer stem cells from oral squamous cell carcinoma: an in vitro FTIRM analysis, Cells 10 (2021) 2127, https://doi.org/10.3390/cells10082127.
[55] V. Notarstefano, M. Pisani, M. Bramucci, L. Quassinti, F. Maggi, L. Vaccari, M. Parlapiano, E. Giorgini, P. Astolfi, A vibrational in vitro approach to evaluate the potential of monoolein nanoparticles as isofuranodiene carrier in MDA-MB 231 breast cancer cell line: new insights from Infrared and Raman microspectroscopies, Spectrochim. Acta Part A: Mol. Biomol. Spectrosc. 269 (2022) 120735, https://doi.org/10.1016/j.saa.2021.120735.
[56] D. Mishra, S. Gade, K. Glover, R. Sheshala, T.R.R. Singh, Vitreous humor: composition, characteristics and implication on intravitreal drug delivery, Curr. Eye Res. 48 (2023) 208–218, https://doi.org/10.1080/02713683.2022.2119254.
[57] P.N. Bishop, M.V. Crossman, D. McLeod, S. Ayad, Extraction and characterization of the tissue forms of collagen types II and IX from bovine vitreous, Biochem. J. 299 (1994) 497–505, https://doi.org/10.1042/bj2990497.
[58] S. Shafaie, V. Hutter, M.B. Brown, M.T. Cook, D.Y.S. Chau, Diffusion through the ex vivo vitreal body – bovine, porcine, and ovine models are poor surrogates for the human vitreous, Int. J. Pharm. 550 (2018) 207–215, https://doi.org/10.1016/j.ijpharm.2018.07.070.

[59] N. Pigaiani, A. Bertaso, E.F. De Palo, F. Bortolotti, F. Tagliaro, Vitreous humor endogenous compounds analysis for post-mortem forensic investigation, Forensic Sci. Int. 310 (2020) 110235, https://doi.org/10.1016/j.forsciint.2020.110235.
[60] J. Dulinska, Z. Setkowicz, K. Janeczko, C. Sandt, P. Dumas, L. Uram, K. Gzielo-Jurek, J. Chwiej, Synchrotron radiation Fourier-transform infrared and Raman microspectroscopy study showing an increased frequency of creatine inclusions in the rat hippocampal formation following pilocarpine-induced seizures, Anal. Bioanal. Chem. 402 (2012) 2267–2274, https://doi.org/10.1007/s00216-011-5488-z.
[61] S. Shariati, G. Khayatian, A new method for selective determination of creatinine using smartphone-based digital image, Microfluid. Nanofluid. 26 (2022) 30, https://doi.org/10.1007/s10404-022-02538-y.
[62] V. Timón, B. Maté, V.J. Herrero, I. Tanarro, Infrared spectra of amorphous and crystalline urea ices, PCCP 23 (2021) 22344–22351, https://doi.org/10.1039/D1CP03503G.
[63] D. Ayodhya, M. Venkatesham, A. Santoshi Kumari, G. Bhagavanth Reddy, G. Veerabhadram, One-pot sonochemical synthesis of CdS nanoparticles: photocatalytic and electrical properties, Int. J. Ind. Chem. 6 (2015) 261–271, https://doi.org/10.1007/s40090-015-0047-7.
[64] A. Zissler, W. Stoiber, P. Steinbacher, J. Geissenberger, F.C. Monticelli, S. Pittner, Postmortem protein degradation as a tool to estimate the PMI: a systematic review, Diagnostics 10 (2020) 1014, https://doi.org/10.3390/diagnostics10121014.
[65] Y. Sorimachi, K. Harada, K. Yoshida, Involvement of calpain in postmortem proteolysis in the rat brain, Forensic Sci. Int. 81 (1996) 165–174, https://doi.org/10.1016/S0379-0738(96)01981-0.
[66] B.H. Stuart, Infrared Spectroscopy: Fundamentals and Applications, Wiley, 2005.
[67] R. Mitchell, C. Charlwood, S.D. Thomas, M. Bellis, N.E.I. Langlois, An audit of the contribution to post-mortem examination diagnosis of individual analyte results obtained from biochemical analysis of the vitreous, Forensic Sci. Med. Pathol. 9 (2013) 515–520, https://doi.org/10.1007/s12024-013-9469-8.
[68] M. Piette, The effect of the post-mortem interval on the level of creatine in vitreous humour, Med. Sci. Law 29 (1989) 47–54, https://doi.org/10.1177/002580248902900107.
[69] N. Ansari, S.K. Menon, Determination of time since death using vitreous humor tryptophan, J. Forensic Sci. 62 (2017) 1351–1356, https://doi.org/10.1111/1556-4029.13430.
[70] E.A. De Letter, M.H.A. Piette, Can routinely combined analysis of glucose and lactate in vitreous humour be useful in current forensic practice? Am. J. Forensic Med. Pathol. 19 (1998) 335–342, https://doi.org/10.1097/00000433-199812000-00008.
[71] C. Petibois, A.-M. Melin, A. Perromat, G. Cazorla, G. Déléris, Glucose and lactate concentration determination on single microsamples by Fourier-transform infrared spectroscopy, J. Lab. Clin. Med. 135 (2000) 210–215, https://doi.org/10.1067/mlc.2000.104460.
[72] E. Wiercigroch, E. Szafraniec, K. Czamara, M.Z. Pacia, K. Majzner, K. Kochan, A. Kaczor, M. Baranska, K. Malek, Raman and infrared spectroscopy of carbohydrates: a review, Spectrochim. Acta A: Mol. Biomol. Spectrosc. 185 (2017) 317–335, https://doi.org/10.1016/j.saa.2017.05.045.
[73] M.F. Rosa, P. Scano, A. Noto, M. Nioi, R. Sanna, F. Paribello, F. De-Giorgio, E. Locci, E. d'Aloja, Monitoring the modifications of the vitreous humor metabolite profile after death: an animal model, Biomed Res. Int. 2015 (2015) 1–7, https://doi.org/10.1155/2015/627201.